DOI: 10.1002/zaac.201000430

Evidence for Tetrahedral Zinc in Amorphous $In_{2-2x}Zn_xSn_xO_3$ (*a*-ZITO)

Cathleen A. Hoel,[a] Sujing Xie,[b] Chris Benmore,[c] Christos D. Malliakas,[a] Jean-François Gaillard,[d] and Kenneth R. Poeppelmeier*[a]

In Memory of Professor Hans Georg von Schnering

Keywords: Transparent conducting oxides; Transparent oxide semiconductor; Zinc indium tin oxide; Absorption spectroscopy; Zinc

Abstract. The structure of amorphous $In_{2-2x}Zn_xSn_xO_3$ (*a*-ZITO, x = 0.2, 0.3, 0.4) was investigated with transmission electron microscopy (TEM), the total scattering pair-distribution function (PDF) and X-ray absorption spectroscopy (XAS), which revealed a well-defined short-range structure that differed from the crystalline bixbyite and corundum ZITO polymorphs. The X-ray absorption near edge structure (XANES) and extended X-ray absorption fine structure (EXAFS) were used to detect InO_6 and SnO_6 octahedra and ZnO_4 tetrahedra in *a*-ZITO, which differ from the InO_6, SnO_6 and ZnO_6 pseudo-octahedra that are observed in the bixbyite and corundum ZITO polymorphs. The formation of the ZnO_4 tetrahedron likely inhibits the crystallization of ZITO when synthesized under mild conditions. in situ XRD showed a gradual transition from *a*-ZITO to a mixture of the bixbyite and corundum ZITO polymorphs as the temperature was raised from 300 °C to 568 °C.

Introduction

Amorphous transparent conducting oxides (TCOs) and transparent oxide semiconductors (TOS) are important materials for flat-panel displays, optoelectronic devices and advanced electronics.[1–3] TCOs and TOSs are integrated into devices as thin films commonly by physical vapor deposition and chemical vapor deposition methods. Deposition conditions, such as temperature, partial oxygen pressure (pO_2) and substrate temperature will influence the film phases, crystallinity and resulting properties.[4–8] Common n-type TCOs, such as tin-doped In_2O_3 (ITO),[9] zinc and tin co-substituted In_2O_3 (ZITO),[10,11] $(ZnO)_kIn_2O_3$ (IZO)[12] and $ZnO{\cdot}SnO_2$ (ZTO),[13,14] exhibit comparable optical and electrical properties for crystalline and amorphous films. *a*-TCOs have several advantages over *c*-TCOs, where "*a*-" denotes "amorphous" and where "*c*-" refers to "crystalline".[15] Mild deposition conditions are utilized such that plastic substrates become a viable option. *a*-TCOs also have low surface roughness for improved interfacial contacts.[16–18] When mechanically stressed, *a*-TCOs undergo less cracking and damage than *c*-TCOs so they can be used in flexible electronic displays.[18–20] Owing to these attractive qualities, *a*-TCOs are being pursued further for transparent electronics and advanced technologies.[3]

Amorphous $In_{2-2x}Zn_xSn_xO_3$ (*a*-ZITO) is a material of particular interest because the conductivity can be tuned from metallic, for application as an *a*-TCO, to semiconducting, for application as an *a*-TOS.[10,20] Significant progress has been made in developing the structure-property relationships of crystalline ITO[21] and ZITO,[7,22] but the structure-property relationships of *a*-ITO and *a*-ZITO are poorly understood owing to a general lack of knowledge of the amorphous structure. Amorphous oxides prove to be challenging and intriguing materials to study because a description of the structure will inevitably be statistical distributions of bond lengths, bond angles and polyhedron connectivities.[23,24] Condensed matter can be described at three structural length scales: short-range order (SRO, < 5 Å), medium-range order (MRO, 5–20 Å), and long-range order (LRO, > 20 Å). The SRO refers to the atomic connectivity and individual polyhedral units, MRO describes the polyhedra connectivities and LRO describes the topology and periodicity. An "amorphous" material, by definition, has no long-range order, but it can exhibit well-defined short-range order.[25–27]

Prior studies have characterized *a*-In_2O_3,[28] *a*-In-Zn-O,[29] and *a*-In-Ga-Zn-O[30,31] thin films using the extended X-ray

* Prof. Dr. K. R. Poeppelmeier
Fax: 01-847-491-7713
E-Mail: krp@northwestern.edu
[a] Department of Chemistry
Northwestern University
2145 Sheridan Rd
Evanston, IL 60208, USA
[b] Materials Science and Engineering
Northwestern University
2020 Cook
Evanston, IL 60208, USA
[c] Advanced Photon Source
Argonne National Laboratory
9700 S. Cass Ave
Lemont, IL 60439, USA
[d] Civil and Environmental Engineering
Northwestern University
2145 Sheridan Rd
Evanston, IL 60208, USA

absorption fine structure (EXAFS) and the pair distribution function (PDF) coupled with computational modelling such as molecular dynamics (MD), reverse Monte Carlo (RMC) and density functional theory (DFT). The characterization of the *a*-In_2O_3 films[28] revealed InO_6 octahedra with an average In-O distance of 2.12 Å compared to the InO_6 octahedra in bixbyite In_2O_3 with an average In–O bond length of 2.18 Å. The In-In distances between the edge and corner-sharing octahedra were close to the In–In distances observed in the bixbyite In_2O_3 structure, but a distribution of In–O–In bond angles was observed in *a*-In_2O_3. Three *a*-In-Zn-O films[29] had been examined with compositions of 10 %, 17 % and 50 % zinc (cation basis). Each composition exhibited the shortened In–O bond length of 2.12 Å that was present in *a*-In_2O_3. The local structure was characterized with InO_6 octahedra and ZnO_4 tetrahedra. Single-phase compounds with compositions of 10 % zinc and 17 % zinc are unknown and $In_2Zn_2O_5$ only forms in the bulk at temperatures above 1550 °C. Both $InGaZnO_4$[30,31] and $In_2Ga_2ZnO_7$[31] are known crystalline compounds that have also been prepared as amorphous films. *Nomura* et al.[30] examined *a*-$InGaZnO_4$ films by EXAFS and reported that zinc preferentially formed tetrahedral coordination environments while gallium and indium occupied fivefold and sixfold coordination sites. *Cho* et al.,[31] however, investigated the local structural of *a*-$InGaZnO_4$ and *a*-$In_2Ga_2ZnO_7$ films and concluded that ZnO_5 bipyramids formed as a result of adjacent InO_6 and GaO_5 polyhedra. This work will focus on probing the short-range structure of *a*-ZITO using local probes that include the total scattering pair distribution function (PDF) and X-ray absorption spectroscopy (XAS). The formation of tetrahedral zinc in this work is significant because, unlike the reports cited above, crystalline ZITO exhibits two polymorphs, both of which adopt ZnO_6 polyhedra.

Results and Discussion

Long-range Structure: Powder X-ray Diffraction

Powder XRD patterns of *a*-ZITO (x = 0.2, 0.3, and 0.4), collected at the J.B. Cohen X-ray facility, showed several diffuse diffraction peaks that varied slightly for each composition. High-resolution XRD patterns of *a*-ZITO (x = 0.2, 0.3, and 0.4), collected at the 11-BM station at the APS, showed primarily diffuse peaks with minor sharp peaks indicative of an amorphous structure with minor crystalline grains present. The positions of the broad peaks coincide with the d-spacings observed for the crystalline bixbyite and corundum polymorphs as shown in Figure 1. The XRD patterns, however, could not be described as a simple physical mixture of poorly crystalline bixbyite and corundum. The average grain size was calculated to be ~14 Å using the Scherrer equation[32] for the most intense peak in *a*-ZITO for x = 0.2 (d = 2.75 Å, K = 0.9), only slightly larger than the bixbyite In_2O_3 unit cell (a = 10 Å) demonstrating the limitation of the information obtained by Rietveld refinement for a poorly crystalline material.

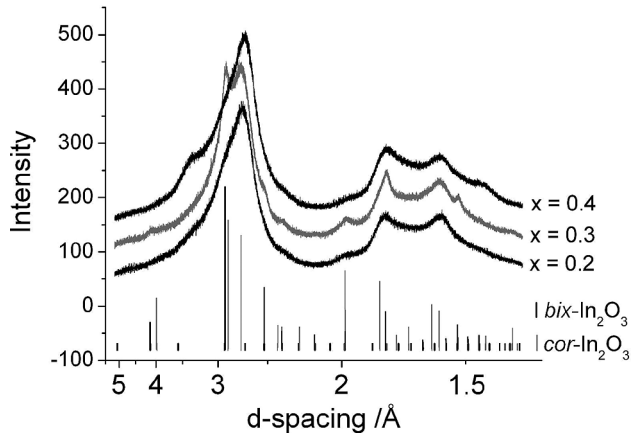

Figure 1. High-resolution XRD of *a*-ZITO with the reflections for bixbyite (#06–0416) and corundum (#22–0336) In_2O_3 drawn in.

Long and Medium-Range Structure: Electron Nanodiffraction and Microscopy

TEM images of *a*-ZITO for x = 0.3 showed irregular aggregated particles that appeared to be approximately 20–50 nm in size (Figure 2a and Figure 2c). The particles were analyzed by selected-area electron diffraction (shown in Figure 2b) and nano-beam diffraction (shown in Figure 2d). Both diffraction

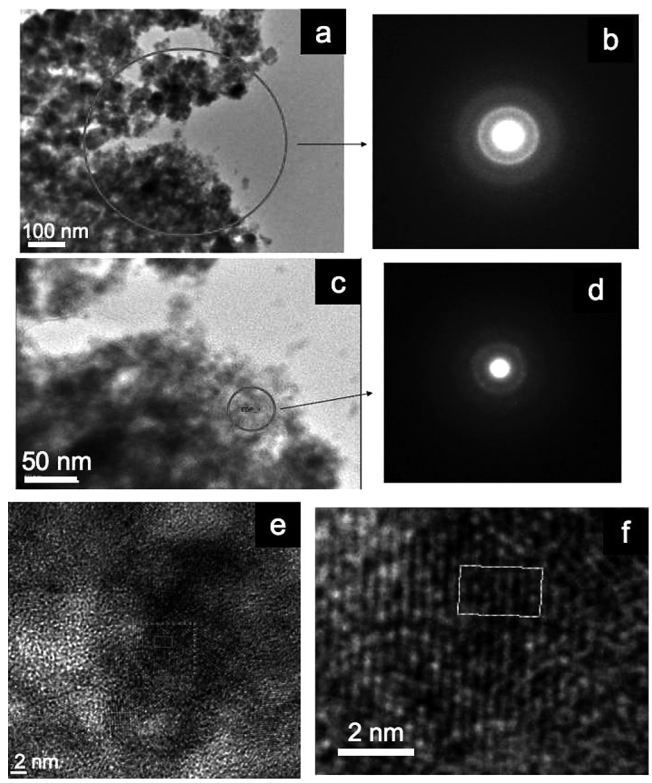

Figure 2. (a, c) TEM images of *a*-ZITO (x = 0.3) and (b, d) the corresponding diffraction patterns such that the beamspot is outlined with a grey circle. (e, f) HREM images of slices of *a*-ZITO (x = 0.3) particles immersed in epoxy resin. Figure 2f is the expansion of the dotted box in Figure 2e. The grey box in e and f is drawn in to show the fringes.

Zeitschrift für anorganische und allgemeine Chemie ZAAC Journal of Inorganic and General Chemistry

patterns (Figure 2b and Figure 2d) consisted of several diffuse halos, characteristic of an amorphous structure. High-resolution TEM images (Figure 2e and Figure 2f) show lattice fringes in small regions. The average distance (± standard deviation) between the fringes for two separate regions was 2.9 ± 0.2 Å and 3.1 ± 0.1 Å while fringes separated by distances of 4–5 Å were also measured. The images show a large number of defects disrupting the lattice fringes preventing long-range order and periodicity.

Medium and Short-Range Structure: Total Scattering Pair Distribution Function

The experimental X-ray pair distribution functions of *a*-ZITO (x = 0.2, 0.3, and 0.4) are plotted in Figure 3 with the calculated PDFs of crystalline bixbyite In_2O_3 (*bix*-In_2O_3) and corundum In_2O_3 (*cor*-In_2O_3). A PDF shows a peak for every pair of atoms separated by the distance r. The PDF of *a*-ZITO showed well-defined short-range structure for atomic pairs separated by distances less than 5 Å. Broadened peaks are evident beyond 5 Å, showing continually decreasing order at higher distances, which is consistent with the broad XRD peaks and diffuse ED rings. PDF captures the average structure of the entire sample while TEM shows individual regimes. Variations of the individual distances between the fringes observed by TEM will appear as a broad distribution in the PDF. The diminishing amplitude with increasing distances between atomic pairs is a result of the increasing structural disorder. The average particle size determined by small angle X-ray scattering (SAXS, see Supporting Information) was 181 Å, using a spherical particle approximation, so particle size will not have a significant effect on the PDF intensity up to 20 Å.

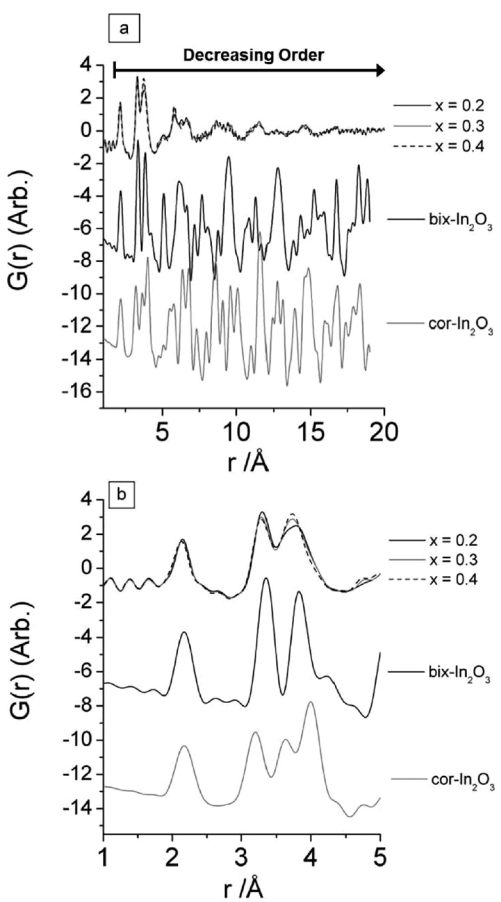

Figure 3. (top) PDF of *a*-ZITO for x = 0.2, x = 0.3 and x = 0.4 in comparison with the calculated PDF of bixbyite In_2O_3 and corundum In_2O_3. (bottom) Expansion of the top plot for the short-range ordered regime, R = 1–5 Å.

The PDFs of *a*-ZITO for x = 0.2, 0.3, and 0.4 are very similar with minor differences in the peak intensities that appear to be systematic. The first peak in *a*-ZITO (x = 0.3) corresponds to the In–O, Sn–O and Zn–O pairs and occurs at an average distance of 2.14 Å. The second and third peaks in *a*-ZITO (x = 0.3) are located at 3.29 Å and 3.73 Å, distances expected for edge and corner-sharing *M*–*M* pairs (*M* = In, Sn, Zn), respectively. The area of the two peaks appears approximately the same implying a similar amount of edge- and corner-sharing polyhedra. The total scattering data of crystalline *bix*-ZITO (x = 0.2, 0.3 and 0.4) were collected under the same conditions to confirm that the broad peaks observed for *a*-ZITO were representative of the structure rather than the measurement conditions. The broadened peaks visible for *a*-ZITO indicate a distribution of *M*–*M* distances and O–*M*–O angles compared to the crystalline analogues. It is likely that this distribution of bond angles associated with the packing of adjacent polyhedra leads to the loss of ordering on the long-range length scale.

Short-Range Structure: X-ray Absorption Spectroscopy

Several restraints were imposed on the EXAFS fits to reduce the number of correlations between the parameters. Constraints were chosen such that they were consistent with the chemical nature of ZITO. Some of the constraints are based on the known crystalline structures. The amorphous structure will inherently exhibit deviation from the crystalline structure, but the degree to which the deviations occur is unknown. Therefore, constraints were chosen in cases where the amorphous structure would be expected to be similar to the crystalline structures. Parameters that were expected to differ between the amorphous and crystalline structures were allowed to float during the fitting routine. The presented fits are first-approximations of the amorphous structure and in order to elucidate further details, more data and experiments would be necessary. It is further emphasized that this is one proposed structural description that is consistent with the EXAFS analysis, but there may be other equally valid representations. Discussion of the parameters and restraints used in each fit is included in the Supporting Information.

In K Edge

The EXAFS is plotted as the $k^2 \cdot \chi(k)$ vs. the modulus of the wavevector and its Fourier transform for *bix*-ZITO, *cor*-ZITO and *a*-ZITO at the In K edge (Figure 4). Previous work confirmed that these EXAFS spectra of *bix*-ZITO[33] and *cor*-ZITO[34] were consistent with the crystallographic structures.

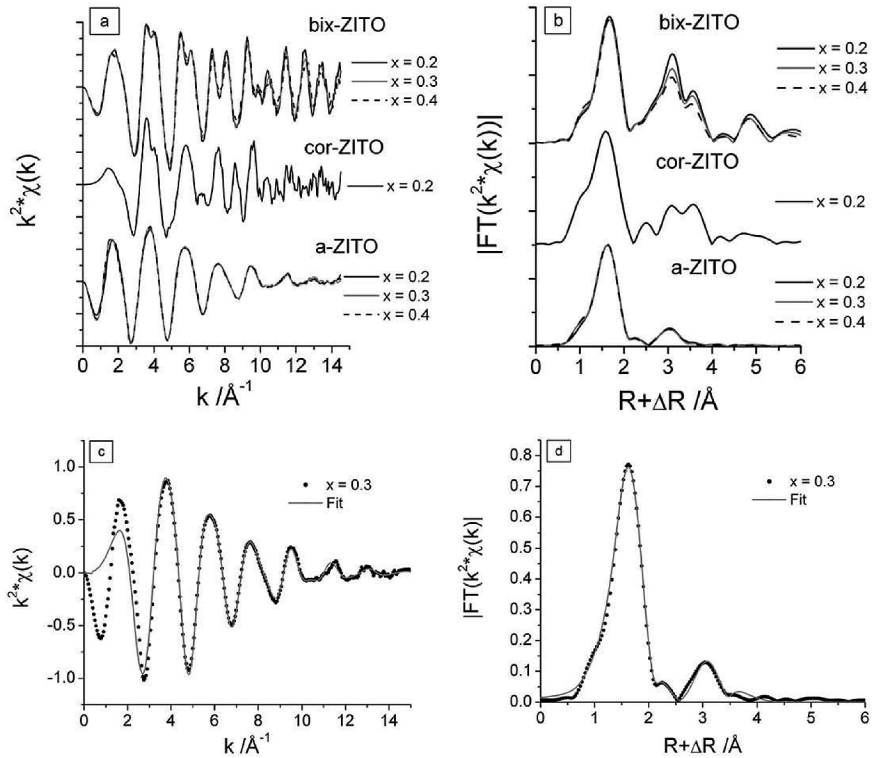

Figure 4. In K edge: **(a)** Plot of $k^2 \cdot \chi(k)$ and **(b)** Fourier transform of *bix*-ZITO, *cor*-ZITO and *a*-ZITO. **(c)** Plot of $k^2 \cdot \chi(k)$ and **(d)** Fourier transform of *a*-ZITO for $x = 0.3$ (black dots) with the best-fit overlaid (solid line).

The amplitudes of the $k^2 \cdot \chi(k)$ and Fourier transform for *bix*-ZITO decrease with increasing zinc and tin substitution.[33] There is little change visible for the *a*-ZITO spectra between $x = 0.2$, 0.3, and 0.4, which suggests the local structure of indium is not dependent on the percentage of zinc and tin.

Four chemical restraints were applied to the fit to reduce correlations between the many EXAFS parameters. The In K edge EXAFS data were fit with only indium neighbors, i.e., zinc and tin were not included in any secondary shells, although it should be mentioned that indium and tin are indistinguishable neighbor types. Although it is unlikely that the second shell is composed only of indium neighbors, the low concentration of zinc and tin and the uncertainty associated with an amorphous structure would prevent zinc and tin from having a significant effect on the indium edge EXAFS signal. This assumption is confirmed by the nearly identical spectra at the indium edge for the compositions at $x = 0.2$, 0.3, and 0.4. The first In–O shell coordination number was set to 6 because indium is preferentially six-coordinate with O, evident by *bix*-In_2O_3 and *cor*-In_2O_3. The total number of cation neighbors in the second shell (3–4 Å) was set to 12 because it is the number of cation neighbors in the bixbyite structure. The number of edge-sharing and corner-sharing indium neighbors were set equal to each other, which is consistent with the PDF. Furthermore, a total of 12 cation neighbors, half edge-sharing and half corner-sharing, is necessary to maintain charge balance with an InO_6 octahedron.

The best fit $k^2 \cdot \chi(k)$ and Fourier transform of *a*-ZITO ($x = 0.3$) at the In K edge are plotted in Figure 4 with the best fit values listed in Table 1. The fitting of the first In-O shell resulted in a distance of 2.14 Å, which is slightly shorter than the average In–O bond length of 2.16 Å in bixbyite ZITO[33] and consistent with the average value of the nearest neighbors detected by the PDF. The edge-sharing neighbors were fit with 3.2 indium at 3.28 Å and 2.8 indium at 3.41 Å. The corner-sharing indium neighbors were fit with 3.2 indium at 3.64 Å and 2.8 indium at 3.88 Å. It should be emphasized that EXAFS detects the average local environment, so the coordination numbers should be interpreted as the relative weighting of an indium neighbor at the given distance. The average distance of the edge-sharing and corner-sharing In-In neighbors is 3.34 Å and 3.75 Å, respectively. The In–In distances determined by EXAFS are close to the *M*–*M* distances observed by PDF with 3.29 and 3.73 Å. The average distances determined from the two spectra are expected to differ because PDF includes every combination of atomic pairs (In–In, In–O, O–O, etc.) while EXAFS previously assumed only In-In pairs.

Table 1. Best fit values of *a*-ZITO ($x = 0.3$) at In K edge. $S_0^2 = \mathbf{1.0}$, $\Delta E_0 = 0.6(7)$ eV, *R*-factor = 0.005.

Neighbor	*R* /Å	C.N.	σ^2 /Å^2
O	2.140(4)	6	0.0083(3)
In	3.28(1)	3.2(4)	0.016(2)
In	3.41(2)	2.8(4)	0.016(2)
In	3.64(1)	3.2(4)	0.016(2)
In	3.88(2)	2.8(4)	0.016(2)

Zeitschrift für anorganische und allgemeine Chemie ZAAC Journal of Inorganic and General Chemistry

Sn K Edge

The EXAFS is plotted as the $k^2 \cdot \chi(k)$ and Fourier transform for *bix*-ZITO, *cor*-ZITO and *a*-ZITO at the Sn K edge for x = 0.2, 0.3, and 0.4 (Figure 5). Prior work demonstrated that the tin local coordination environment for *bix*-ZITO was consistent with the bixbyite structure[33] and *cor*-ZITO was consistent with the corundum structure.[34] The tin substituent exhibited a first shell Sn–O bond contraction in *bix*-ZITO and *cor*-ZITO owing to the small Sn^{4+} radius.[33,34] The EXAFS of crystalline *bix*-ZITO at the Sn edge exhibited an amplitude reduction as a function of x, which has been attributed to increased zinc substitution in the neighboring cation shells.[33] The EXAFS of *a*-ZITO, on the other hand, shows minor variations as a function of x, which suggests the local structure has a mild sensitivity to the composition.

The best fit $k^2 \cdot \chi(k)$ and Fourier transform are plotted in Figure 5 and the best fit values of the Sn K edge EXAFS are listed in Table 2. The EXAFS of *a*-ZITO (x = 0.3) was fit with only indium neighbors for r = 3–4 Å. It is unlikely that tin has only indium neighbors, but the low concentration of zinc and tin coupled with the distribution of bond lengths associated with an amorphous structure will prevent zinc and tin from having a significant effect on the net EXAFS signal. The coordination number of the first Sn–O shell was set to 6 because Sn^{4+} is preferentially octahedral with O, as demonstrated by rutile SnO_2. The first shell Sn–O distance in *a*-ZITO was found to be 2.06 Å, which is close to that of *bix*-ZITO at 2.08 Å, *cor*-ZITO at 2.08 Å and SnO_2 at 2.06 Å.[33,34] The cation neighbors were composed of 4.1 indium at 3.27 Å, 3.0 indium at 3.48 Å and 3.9 indium at 3.72 Å. It is notable how the *a*-ZITO short-range structure of tin is quite different from the short-range structure of indium.

Table 2. Best fit values of *a*-ZITO (x = 0.3) at Sn K edge. S_0^2 = **1.0**, ΔE_0 = 1.2(5) eV, *R*-factor = 0.002.

Neighbor	R /Å	C.N.	σ^2 /Å^2
O	2.058(3)	6	0.0045(2)
In	3.265(6)	4.1(4)	0.0091(7)
In	3.48(1)	3.0(2)	0.0091(7)
In	3.724(9)	3.9(4)	0.0091(7)

Zn K Edge

The X-ray absorption near edge structure (XANES) of the Zn K edge for *a*-ZITO was first examined because zinc can exhibit octahedral coordination, as in *bix*-ZITO and *cor*-ZITO, and tetrahedral coordination, as in ZnO. The XANES spectra of the Zn K edge for *bix*-ZITO, *cor*-ZITO, ZnO and *a*-ZITO are plotted in Figure 6. The XANES regime shows the empty density of states of the absorbing element coupled with oscillations that are caused by single and multiple scattering of the photoelectron. The peak at the Zn K edge is attributed to the 1s → 4p transition.[35] The peak shape will depend on the neighboring elements, arrangement and ligand distance.[35,36] *Waychunas* et al.[37] simulated the XANES spectra at the Zn K

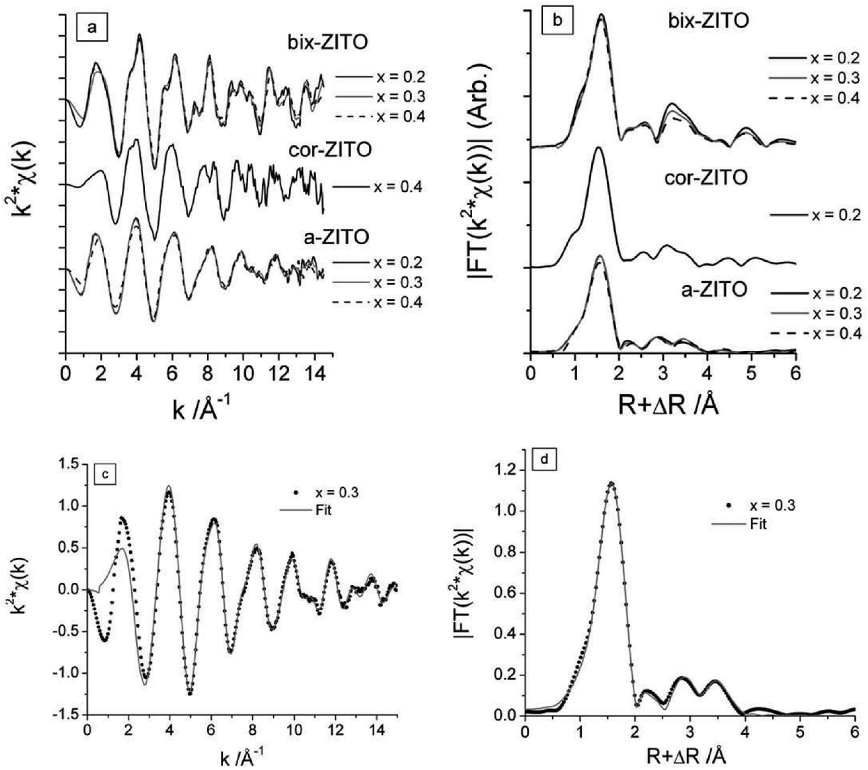

Figure 5. Sn K edge: **(a)** Plot of $k^2 \cdot \chi$ (k) and **(b)** Fourier transform of *bix*-ZITO, *cor*-ZITO and *a*-ZITO. **(c)** Plot of $k^2 \cdot \chi(k)$ and **(d)** Fourier transform of *a*-ZITO for x = 0.3 (black dots) with the best-fit overlaid (solid line).

edge of clusters with ZnO_4 or ZnO_6 polyhedra. The XANES spectrum of an isolated ZnO_4 tetrahedron showed less intensity for the peak at the edge (the "white line") and a broader decay compared to an isolated ZnO_6 octahedron. The XANES spectrum of *a*-ZITO at the Zn K edge shows a low-intensity white line followed by a broad decay, which suggests zinc is tetrahedrally coordinated by oxygen atoms. Furthermore, the XANES spectrum of the Zn K edge is featureless, meaning the extended structure is too disordered to generate significant single or multiple scattering resonances.

The EXAFS are plotted as the $k^2{\cdot}\chi(k)$ and Fourier transform for *bix*-ZITO, *cor*-ZITO and *a*-ZITO (Figure 7). Prior work demonstrated that the zinc local coordination environment for *bix*-ZITO was consistent with the bixbyite structure[33] and *cor*-ZITO was consistent with the corundum structure.[34] The EXAFS of crystalline *bix*-ZITO at the Zn edge exhibited an amplitude reduction as a function of zinc and tin substitution (x), which had been attributed to increasing zinc substitution in the neighboring cation shells.[33] The EXAFS of *a*-ZITO, on the other hand, shows a strong first shell and no coherent coordination shells past 2 Å for x = 0.2, 0.3, and 0.4, consistent with the featureless XANES. The Zn–O first shell of *a*-ZITO (x = 0.3) was fit with 4 O at 1.97(2) Å where S_0^2 = 1.0, σ^2 = 0.010(1) Å^2 and ΔE_0 = 0.2(1.8) eV (R-factor = 0.011). The Zn–O bond length of 1.97 Å is consistent with that of four-coordinate zinc. Longer bond lengths of 2.06 Å or 2.12 Å, would suggest a five- or six-coordinate environment, respectively.[38] The EXAFS data are consistent with a Zn–O coordination number of 4 and not 6, which corroborates the tetrahedral coordination of zinc inferred from the XANES spectrum.

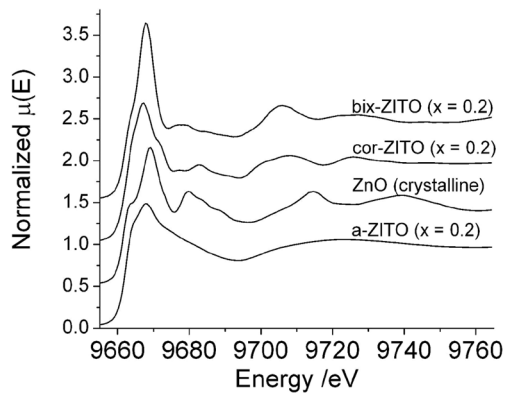

Figure 6. X-ray absorption near edge structure (XANES) of *bix*-ZITO, *cor*-ZITO, ZnO and *a*-ZITO at the Zn K edge.

Crystallization of a-ZITO: in-situ and ex-situ X-ray Diffraction

The precursor was heated from room temperature to 568 °C while the phases were monitored in situ by powder X-ray diffraction (Figure 8). Room temperature XRD verified that the precursor was $In_{0.7}Zn_{0.15}Sn_{0.15}(OH)_3$ (x = 0.3). Upon heating, the peaks indicative of the precursor diminished and once the sample reached 300 °C the amorphous structure was observed. The temperature was held at 300 °C for 1 hour and no change

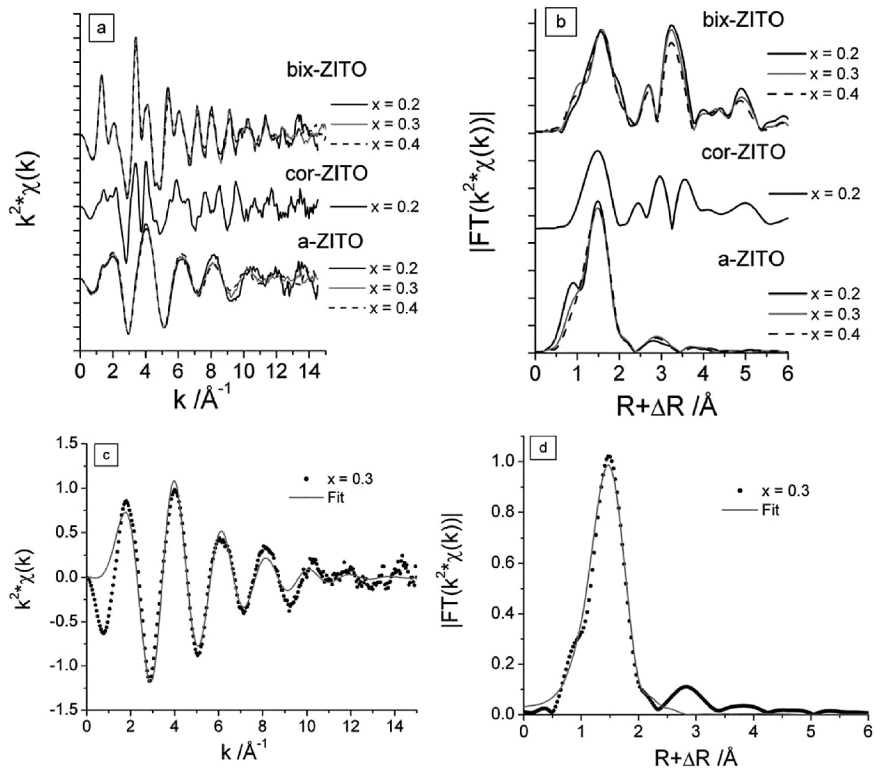

Figure 7. Zn K edge: **(a)** Plot of $k^2{\cdot}\chi(k)$ and **(b)** Fourier transform of *bix*-ZITO, *cor*-ZITO and *a*-ZITO. **(c)** Plot of $k^2{\cdot}\chi(k)$ and **(d)** Fourier transform of *a*-ZITO for x = 0.3 (black dots) with the best-fit overlaid (solid line).

Zeitschrift für anorganische und allgemeine Chemie ZAAC Journal of Inorganic and General Chemistry

was observed in the XRD pattern. As the temperature rose to 568 °C the XRD patterns showed the gradual transition from an amorphous to a crystalline structure with peaks forming and sharpening indicative of growing grains. The sample was held between 560–570 °C for an hour while the grain size started to plateau. The final diffraction peaks corresponded to a mixture of bixbyite and corundum ZITO.

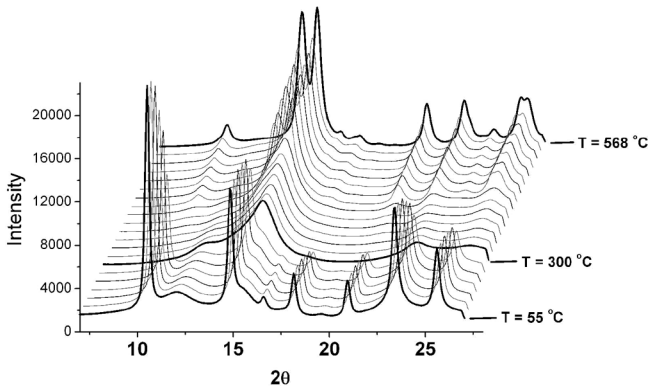

Figure 8. XRD patterns measured in-situ as a function of temperature starting with $In_{0.7}Zn_{0.15}Sn_{0.15}(OH)_3$ precursor at 55 °C and heating to *a*-ZITO at 300 °C (black trace) followed by crystallization to a mixture of bixbyite and corundum ZITO at 568 °C.

a-ZITO for $x = 0.2$, 0.3, and 0.4 were heated to 700 °C to examine the products upon crystallization. A mixture of the bixbyite and corundum polymorphs was observed by XRD as shown in Figure 9. As the percentage of zinc and tin increased, a higher percentage of corundum formed over bixbyite. *Gurlo* et al.[39] reported increased formation of the corundum polymorph with increased Fe substitution when $In_{2-y}Fe_yO_3$ was synthesized by co-precipitation and calcination. The addition of smaller cations has been attributed to stabilization of the more dense corundum structure,[39,40] consistent with increasing corundum ZITO for increasing *x*.

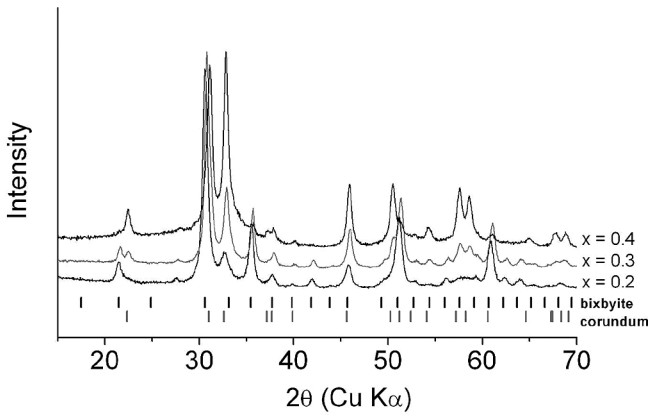

Figure 9. XRD patterns of crystallized products after heating *a*-ZITO to 700 °C for 2 hours for $x = 0.2$, $x = 0.3$ and $x = 0.4$.

The appearance of the four-coordinate zinc could suggest that *a*-ZITO is a physical mixture of *a*-ITO and *a*-ZnO. The experimental evidence, however, does not support the presence of *a*-ZnO. The Zn edge EXAFS, shown in Figure 10, is not consistent with *a*-ZnO. The EXAFS spectrum of crystalline ZnO has a strong second shell, which consists of 12 zinc neighbors, as shown in Figure 10. A reduced coordination number and increased MSRD would still lead to a noticeable second shell. The EXAFS spectrum of *a*-ZITO, on the other hand, shows a trace second shell indicating that ZnO is not present as a secondary amorphous phase. It should also be noted that separate syntheses of ITO and ZnO under these synthesis conditions yield crystalline ITO and ZnO. Therefore, it is unlikely that the structure of *a*-ZITO is a physical mixture of *a*-ITO and *a*-ZnO.

The presence of the ZnO_4 unit is the distinguishing difference between the *a*-ZITO local structure and the crystalline *bix*-ZITO and *cor*-ZITO local structures. The formation of the ZnO_4 tetrahedron likely stabilizes the amorphous structure and prevents crystallization to a mixture of bixbyite and corundum ZITO. The necessity of zinc to stabilize the amorphous structure is evident as the calcination of $In(OH)_3$ at 300 °C led to crystalline *bix*-In_2O_3. Calcination of $In(OH)_3$ at lower temperatures, such as 250 °C, yielded a mixture of $In(OH)_3$ and *bix*-In_2O_3; amorphous In_2O_3 was not observed. The direct conversion of unsubstituted $In(OH)_3$ to *bix*-In_2O_3 has been confirmed by *in situ* XRD.[41]

Conclusions

A summary of the different characterization techniques and the results is listed in Table 3. The primary structural units in *a*-ZITO were InO_6, SnO_6 and ZnO_4 polyhedra in contrast to the InO_6, SnO_6 and ZnO_6 units that are observed in crystalline *bix*-ZITO and *cor*-ZITO. The XRD, PDF and EXAFS all suggest that the structure of *a*-ZITO differs from a physical mixture of *bix*-ZITO and *cor*-ZITO. The unique short-range structure of *a*-ZITO is consistent with the formation of ZnO_4 tetrahedra, which inhibit nucleation of the *bix*-ZITO and *cor*-ZITO phases. Furthermore, structural order on the long range was prohibited by the formation of a wide distribution of O–*M*–O bond angles (*M* = In, Sn, Zn). Higher temperatures favored a crystalline structure, which led to the formation of the bixbyite and corundum polymorphs characterized by ZnO_6 octahedra. The structural information learned from this study, in particular the formation of tetrahedral ZnO_4 to stabilize the amorphous structure, can be used as a basis to begin to understand the origin of the optical and electrical properties observed for *a*-ZITO.

Experimental Section

Synthesis

The synthesis of *a*-ZITO is a two-step process: precipitation followed by calcination. Aqueous stock solutions of each metal were prepared by dissolving $In(NO_3)_3{\cdot}xH_2O$, $SnCl_4$ or $ZnCl_2$ in deionized water and determining the precise concentration with ICP-AES. The synthesis was carried out for three [In]:[Sn]:[Zn] ratios: 0.8:0.1:0.1 ($x = 0.2$), 0.7:0.15:0.15 ($x = 0.3$) and 0.6:0.2:0.2 ($x = 0.4$). The solution was diluted such that the total metallic concentration ([In]+[Sn]+[Zn]) was

Dedicated Issue

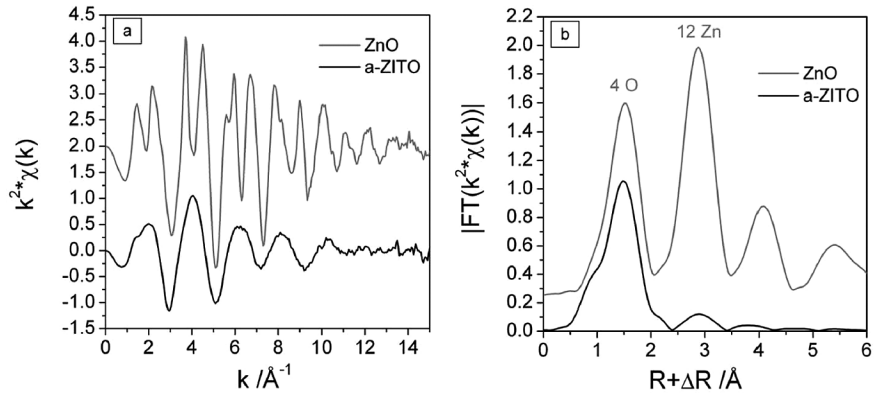

Figure 10. $k^2{\cdot}\chi$ (k) spectra and **(b)** k^2-weighted Fourier transform of *a*-ZITO at $x = 0.3$ (black) compared to ZnO (grey).

Table 3. Summary of results from structural characterization techniques.

Method	Length Scale	Degree of Order	Results
XRD	> 20 nm	Disordered	–
ED	50 nm	Disordered	–
TEM	> 2 nm	Disordered	–
TEM	1–2 nm	Ordered regimes	–
PDF (MRO)	5–20 Å	Decreasing order	–
PDF (SRO)	1–5 Å	Ordered	*M*–O 2.14 Å
			M–*M* 3.29 Å
			M–*M* 3.73 Å
EXAFS (In edge)	1–4 Å	Ordered	In–O 2.14 Å
			In–In 3.28 Å
			In–In 3.41 Å
			In–In 3.64 Å
			In–In 3.88 Å
EXAFS (Sn edge)	1–4 Å	Ordered	Sn–O 2.06 Å
			Sn–In 3.27 Å
			Sn–In 3.48 Å
			Sn–In 3.72 Å
EXAFS (Zn edge)	1–2 Å	Ordered	Zn–O 1.97 Å
EXAFS (Zn edge)	2–4 Å	Disordered	–

0.08 M. For the solutions with high concentrations of tin and zinc it was necessary to add several drops concentrated HCl or HNO_3 to keep the cations dissolved. The metal solution (10 mL, 0.08 m) was added dropwise to $NaOH_{(aq)}$ (100 mL, 6 mM, pH ≈ 11) in air while the pH of the solution was maintained above 10.3 by small additions of $NaOH_{(aq)}$ (1.2 M) using a pH-stat based on an ABU9x autotitrator (Radiometer). A white precipitate formed instantly upon addition of the metal solution to the $NaOH_{(aq)}$ solution. After the addition of the entire metal solution the reaction beaker was covered with Parafilm™ and left to stir overnight. The mixture was then centrifuged to separate the precipitate from the mother liquor. The precipitate was rinsed with deionized water three times, separated by centrifugation and the solid was dried at 80 °C overnight to obtain the precursor (see Supporting Information for characterization of the precursor). The dried precursor was ground to a powder and calcined at 300 °C overnight to obtain amorphous ZITO, which was a yellow color. Thermogravimetric analysis of the precursor verified that a weight loss occurred just above 200 °C (see Supporting Information). The O-H stretch that was observed for the precursor by attenuated total reflection infrared (ATR-IR) spectroscopy was absent for the amorphous oxide (see Supporting Information).

X-ray Diffraction

Powder X-ray diffraction (XRD) patterns were collected at the J.B. Cohen X-ray Facility at Northwestern University using a Rigaku diffractometer (Tokyo) with Ni-filtered Cu-K_α radiation over the range $2\theta = 15$–$70°$ with a 0.05° step size and 1 second dwell time. High-resolution powder XRD (HR-XRD) patterns were obtained from Sector 11 BM-B at the Advanced Photon Source at Argonne National Laboratory (ANL-APS) using an average wavelength of 0.4586 Å. Discrete detectors covering an angular 2θ range from –6 to 16° were scanned over a 34° range, with data points collected every 0.001° 2θ at a scan speed of 0.01°/s. Two NIST standard reference materials, Si (SRM 640c) and Al_2O_3 (SRM 676) were used to calibrate the instrument, where the Si lattice constant determines the wavelength for each detector.

High-energy total X-ray scattering data, which were used for PDF analysis, were collected at Sector 6 ID-D of the APS at ANL. The beam energy was selected at 87.06 keV and the data were collected in transmission on a Mar345 Image plate. The detector distance was calibrated with a Si-NIST standard. The sample was loaded into a Kapton capillary tube with a 1 mm diameter. A background pattern was collected from an empty Kapton capillary tube and used for the correction. Each measurement was replicated 5 times to improve counting statistics. The 2-D XRD patterns were merged and integrated with Fit2D[42,43] to 1-D patterns. PDFgetX2[44] was used to removed the background and convert the integrated XRD pattern to the structure function $S(Q)$, where $S(Q) = 1+|I^{coh}(Q)-\Sigma_i c_i f_i^2(Q)|/|\Sigma_i c_i f_i^2(Q)|$ such that $I^{coh}(Q)$ is the coherent X-ray scattering, c_i is the atomic concentration of species i and $f_i(Q)$ is the X-ray scattering factor. The pair distribution function, $G(r)$, is extracted by a Fourier transform of $Q[S(Q)–1]$ from $Q = 0.5$–26.0 Å^{-1}. The pair distribution function can also be expressed as $G(r) = 4\pi r[\rho(r)–\rho_0]$ where r is the interatomic distance, $\rho(r)$ is the local electron density and ρ_0 is the average electron density.

Powder XRD was obtained in situ while heating a pellet of precursor from room temperature to 568 °C. The data were collected at the ANL-APS Sector 5-BM-D. The wavelength was selected as 0.654 Å with a double-crystal Si(111) monochromator and a sagittal bender was inserted up-stream to focus the beamspot to a 2 mm diameter. The $In_{0.7}Zn_{0.15}Sn_{0.15}(OH)_3$ precursor was mixed with a 10 % aqueous solution of polyvinyl alcohol to act as a binder and pressed into a pellet 1.3 cm in diameter and approximately 0.38 mm thick. The pellet was placed in a Linkam Optical DSC Thermatica system and heated from room temperature to 568 °C. Transmission XRD data were obtained

Zeitschrift für anorganische und allgemeine Chemie ZAAC Journal of Inorganic and General Chemistry

with a selected energy beam and Mar165 Image plate detector. The 2D XRD patterns were calibrated and integrated with the program Fit2D.[42,43] The wavelength and detector distance were calibrated with a LaB_6-NIST standard to be 0.654 Å and 160.7 mm, respectively.

X-ray Absorption Spectroscopy

The ZITO samples and In_2O_3, SnO_2 and ZnO standards were prepared for EXAFS measurements by spreading a uniform layer of the powder onto low-absorbing adhesive tape and adjusting the number of stacked layers to obtain $\mu \approx 2$ and $\Delta\mu_0(E) \approx 1$. The XAS data for the crystalline bixbyite and corundum polymorphs of ZITO (*bix*-ZITO and *cor*-ZITO) have been previously reported.,[33][34]

The X-ray absorption spectra were measured at the ANL-APS facility operating at 100 mA and 7.0 GeV. The double-crystal monochromator consisted of parallel Si(111) crystals, which were detuned to 70 % of the maximum beam intensity to reject higher order harmonics. Each measurement included an indium, tin or zinc metal foil reference to calibrate the absorption edge energy. The edge energy was chosen at the inflection point – where the second derivative equals zero. The edge energies were set at 27940 eV for indium, 29200 eV for tin and 9659 eV for zinc. The standards and the samples at the In, Sn, and Zn edges were measured in transmission mode using Oxford ionization chambers with a path length of 30 cm. The chambers were filled with gas mixtures of He, N_2, and Ar to obtain 10 % absorption for the incident beam, I_0, 20 % absorption for the sample transmitted beam, I_T, and 60 % absorption for the reference foil transmitted beam, I_{T2}. The Sn measurements were replicated 25 times and the Zn measurements were replicated 5 times to improve counting statistics (See Supporting Information for details of the background removal and fitting procedure).

Background removal was performed using the AutoBK algorithm[45,46] as implemented in Athena,[47] a graphical front-end for the IFFEFIT[47–49] software package. The data were normalized to an edge step height of one. The first inflection point of the absorption edge defined the edge energy, E_0, which was used to determine the modulus of the photoelectron wave number: $k = \sqrt{2m_e(E-E_0)/\hbar^2}$ where m_e is the electron mass, $\hbar$ is the reduced Planck's constant, and E is the incident X-ray energy. Both the samples and standards were measured from 250 eV below the edge to 1230 eV above the In and Sn K edge (k = 18 Å^{-1}). The samples and standards were measured from 150 eV below the edge to 1230 eV above the Zn K edge. The $\chi(k)$ spectra was Fourier transformed with a sine window over the region k = 3.3–12.5 Å^{-1} for the In data, k = 3.6–12.25 Å^{-1} for the Sn data and k = 2.4–9.8 Å^{-1} for the Zn data. Fitting and simulations of the EXAFS spectra were performed using the FEFF 6.0 code[50] as implemented in Artemis. The goodness-of-fit was determined by minimizing the residual component, $R = \Sigma_i(\text{data}_i - \text{fit}_i)^2 / \Sigma_i \text{data}_i^2$, between the model and experimental values. The fitting was carried out in real space over the ranges R = 1.1–3.6 Å for indium, R = 1.1–4.0 Å for Sn and R = 1.1–2.1 Å for the Zn data. All Fourier transforms are shown uncorrected for phase shifts.

Electron Diffraction and Microscopy

The *a*-ZITO (x = 0.3) powder was embedded in epoxy resin and sectioned using a LKB 2188 Ultratome Nova microtome and glass knife. Sections were cut at about 100 nm thick and loaded onto holey-carbon copper grids. A JEOL JEM-2100F transmission electron microscope (Tokyo, Japan) was used to study the structure and composition distribution of *a*-ZITO. The microscope is operated at 200 kV with a Schottky field emission gun. EDS analysis was performed in the scanning transmission electron microscopy (STEM) mode to reveal the composition distribution. The structure was characterized by selected area-electron diffraction and nano-beam diffraction.

Supporting Information (see footnote on the first page of this article): X-ray diffraction, thermogravimetric analysis and attenuated total reflectance infrared spectroscopy of the precursor; energy dispersive spectroscopy mapping of *a*-ZITO (x = 0.3); small angle X-ray scattering of *a*-ZITO (x = 0.4); discussion of EXAFS fitting constraints and analysis.

Acknowledgement

C.A.H. was funded through the Materials Research Science and Engineering Center at Northwestern University supported by the National Science Foundation under NSF Award Number DMR-0520513. The amorphous ZITO work is based upon work supported as part of ANSER, an Energy Frontier Research Center funded by the U.S. Department of Energy, Office of Science, Office of Basic Energy Sciences under Award Number DE-SC0001059. The authors gratefully acknowledge additional support from the Department of Energy Basic Energy Sciences (Award No. DE-FG02–08ER46536, crystalline ZITO work). The XAS and in-situ XRD was performed at the Du-Pont-Northwestern-Dow Collaborative Access Team (DND-CAT) located at Sector 5 of the Advanced Photon Source (APS). DND-CAT is supported by E.I. Dupont de Nemours & Co., The Dow Chemical Company and the State of Illinois. Use of the APS was supported by the US Department of Energy, Office of Science, Office of Basic Energy Sciences, under Contract No. DE-AC02–06CH11357. The authors thank Dr. Qing Ma for assistance with the XAS and in-situ XRD measurements and helpful discussions and the 11-BM staff for the HR-XRD measurements. The MU-CAT sector 6 at the APS is supported by the Department of Energy, Office of Science through the Ames Laboratory Contract No· W-7405-Eng-82. C.A.H. and K.R.P. thank T.O. Mason and D. Proffit for helpful discussions. The electron microscopy was performed in the EPIC facility of *NU*ANCE Center at Northwestern University. *NU*ANCE Center is supported by NSF-NSEC, NSF-MRSEC, Keck Foundation, the State of Illinois, and Northwestern University. This work made use of the J.B. Cohen X-ray Facility supported by the MRSEC program of the National Science Foundation (DMR-0520513) at the Materials Research Center of Northwestern University. This work (ICP-AES measurements) made use of the Integrated Molecular Structure Education and Research Center (IMSERC) supported by the National Science Foundation using grant DMR-0520513.

References

[1] P. P. Edwards, A. Porch, M. O. Jones, D. V. Morgan, R. M. Perks, *Dalton Trans.* **2004**, 2995.
[2] E. Fortunato, D. Ginley, H. Hosono, D. C. Paine, *MRS Bull.* **2007**, *32*, 242.
[3] J. F. Wager, D. A. Keszler, R. E. Presley, in: *Transparent Electronics*, Springer, New York, **2008**,.
[4] R. B. H. Tahar, T. Ban, Y. Ohya, Y. Takahashi, *J. Appl. Phys.* **1998**, *83*, 2631.
[5] E. B. Ali, H. E. Maliki, J. C. Bernede, M. Sahnoun, A. Khelil, O. Saadane, *Mater. Chem. Phys.* **2002**, *73*, 78.
[6] F. O. Adurodija, L. Semple, R. Bruning, *Thin Solid Films* **2005**, *492*, 153.

[7] S. P. Harvey, T. O. Mason, D. B. Buchholz, R. P. H. Chang, C. Korber, A. Klein, *J. Am. Ceram. Soc.* **2008**, *91*, 467.
[8] S. Kaleemulla, A. S. Reddy, S. Uthanna, P. S. Reddy, *J. Alloys Compd.* **2009**, *479*, 589.
[9] J. R. Bellingham, W. A. Phillips, C. J. Adkins, *J. Phys.: Condens. Matter* **1990**, *2*, 6207.
[10] D. B. Buchholz, J. Liu, T. J. Marks, M. Zhang, R. P. H. Chang, *ACS Appl. Mater. Interfaces* **2009**, *1*, 2147.
[11] C. A. Hoel, T. O. Mason, J.-F. Gaillard, K. R. Poeppelmeier, *Chem. Mater.* **2010**, *22*, 3569.
[12] T. Moriga, M. Mikawa, Y. Sakakibara, Y. Misaki, K.-i. Murai, I. Nakabayashi, K. Tominaga, J. B. Metson, *Thin Solid Films* **2005**, *486*, 53.
[13] T. Minami, H. Sonohara, S. Takata, H. Sato, *Jpn. J. Appl. Phys. Part 2*, **1994**, *33*, L1693.
[14] J. D. Perkins, J. A. del Cuerto, J. L. Alleman, C. Warmsingh, B. M. Keyes, L. M. Gedvilas, P. A. Parilla, B. To, D. W. Readey, D. S. Ginley, *Thin Solid Films* **2002**, *411*, 152.
[15] T. Kamiya, H. Hosono, *NPG Asia Mater.* **2010**, *2*, 15.
[16] M. P. Taylor, D. W. Readey, M. F. A. M. van-Hest, C. W. Teplin, J. L. Alleman, M. S. Dabney, L. M. Gedvilas, B. M. Keyes, B. To, J. D. Perkins, D. S. Ginley, *Adv. Funct. Mater.* **2008**, *18*, 3169.
[17] J.-A. Jeong, H.-K. Kim, S.-I. Na, *Electrochem. Solid-State Lett.* **2009**, *12*, J80.
[18] D. Y. Lee, G. H. Lee, P. K. Song, *Jpn. J. Appl. Phys.* **2009**, *48*, 05EC03.
[19] G.-S. Heo, Y. Matsumoto, I.-G. Gim, J.-W. Park, G.-Y. Kim, T.-W. Kim, *Jpn. J. Appl. Phys.* **2010**, *49*, 035801.
[20] J. Liu, D. B. Buchholz, R. P. H. Chang, A. Facchetti, T. J. Marks, *Adv. Mater.* **2010**, *22*, 2333.
[21] G. Frank, H. Kostlin, *Appl. Phys. A* **1982**, *27*, 197.
[22] D. E. Proffit, D. B. Buchholz, R. P. H. Chang, M. J. Bedzyk, T. O. Mason, Q. Ma, *J. Appl. Phys.* **2009**, *106*, 113524.
[23] S. R. Elliott, in: *Physics of Amorphous Materials*, John Wiley & Sons, Inc., New York, **1990**,.
[24] S. R. Elliott, *Nature* **1991**, *354*, 445.
[25] G. N. Greaves, A. Fontaine, P. Lagarde, D. Raoux, S. J. Gurman, *Nature* **1981**, *293*, 611.
[26] L. Cormier, L. Galoisy, G. Calas, *Europhys. Lett.* **1999**, *45*, 572.
[27] L. A. Aleshina, S. V. Loginova, *Crystallogr. Rep.* **2002**, *48*, 531.
[28] F. Utsuno, H. Inoue, I. Yasui, Y. Shimane, S. Tomai, S. Matsuzaki, K. Inoue, I. Hirosawa, M. Sato, T. Honma, *Thin Solid Films* **2006**, *496*, 95.
[29] F. Utsuno, H. Inoue, Y. Shimane, T. Shibuya, K. Yano, K. Inoue, I. Hirosawa, M. Sato, T. Honma, *Thin Solid Films* **2008**, *516*, 5818.
[30] K. Nomura, T. Kamiya, H. Ohta, T. Uruga, M. Hirano, H. Hosono, *Phys. Rev. B* **2007**, *75*, 035212.
[31] D.-Y. Cho, J. Song, K. D. Na, C. S. Hwang, J. H. Jeong, J. K. Jeong, Y.-G. Mo, *Appl. Phys. Lett.* **2009**, *94*, 112112.
[32] A. L. Patternson, *Phys. Rev.* **1939**, *56*, 978.
[33] C. A. Hoel, J.-F. Gaillard, K. R. Poeppelmeier, *J. Solid State Chem.* **2010**, *183*, 761.
[34] C. A. Hoel, J. M. G. Amores, E. Moran, M. A. Alario-Franco, J.-F. Gaillard, K. R. Poeppelmeier, *J. Am. Chem. Soc.* **2010**, *132*, 16479.
[35] P. Glatzel, G. Smolentsev, G. Bunker, *J. Phys. A* **2009**, *190*, 012046.
[36] G. Bunker, *Phys. B* **1989**, *158*, 259.
[37] G. A. Waychunas, C. C. Fuller, J. A. Davix, J. J. Rehr, *Geochim. Cosmochim. Acta* **2003**, *67*, 1031.
[38] R. D. Shannon, *Acta Crystallogr., Sect. A* **1976**, *32*, 751.
[39] A. Gurlo, M. Ivanovskaya, N. Barsan, U. Weimar, *Inorg. Chem. Commun.* **2003**, *6*, 569.
[40] C. T. Prewitt, R. D. Shannon, D. B. Rodgers, A. W. Sleight, *Inorg. Chem.* **1969**, *8*, 1985.
[41] L. Schlicker, R. Riedel, A. Gurlo, *Nanotechnology* **2009**, *20*, 495702.
[42] A. P. Hammersley, *High Pressure Res.* **1996**, *14*, 235.
[43] A. P. Hammersley, *Fit2D: An Introduction and Overview*, ESRF97HA02T, **1997**.
[44] X. Qiu, J. W. Thompson, S. J. L. Billinge, *J. Appl. Crystallogr.* **2004**, *37*, 678.
[45] M. Newville, P. Livins, Y. Yacoby, J. J. Rehr, E. A. Stern, *Jpn. J. Appl. Phys. Part I* **1993**, *32(Supplement)*, 125.
[46] B. Ravel, M. Newville, J. O. Cross, C. E. Bouldin, *Phys. B* **1995**, *209*, 145.
[47] B. Ravel, M. Newville, *J. Synchrotron Radiat.* **2005**, *12*, 537.
[48] M. Newville, *J. Synchrotron Radiat.* **2001**, *8*, 96.
[49] M. Newville, *J. Synchrotron Radiat.* **2001**, *8*, 322.
[50] J. J. Rehr, S. I. Zabinsk, *FEFF5: An* ab initio *Multiple Scattering XAFS Code*, Department of Physics; University of Washington, **1992**.

Received: December 10, 2010
Published Online: June 7, 2011

